BIOMICROFLUIDICS **7**, 011809 (2013)

Investigating dielectric properties of different stages of syngeneic murine ovarian cancer cells

Alireza Salmanzadeh,[1,2] Michael B. Sano,[1] Roberto C. Gallo-Villanueva,[1] Paul C. Roberts,[3] Eva M. Schmelz,[4,a)] and Rafael V. Davalos[1,2,a)]
[1]*School of Biomedical Engineering and Sciences, Virginia Tech-Wake Forest University, Blacksburg, Virginia 24061, USA*
[2]*Department of Engineering Science and Mechanics, Virginia Tech, Blacksburg, Virginia 24061, USA*
[3]*Department of Biomedical Sciences and Pathobiology, Virginia Tech, Blacksburg, Virginia 24061, USA*
[4]*Human Nutrition, Foods, and Exercise, Virginia Tech, Blacksburg, Virginia 24061, USA*

(Received 15 September 2012; accepted 8 January 2013; published online 23 January 2013)

In this study, the electrical properties of four different stages of mouse ovarian surface epithelial (MOSE) cells were investigated using contactless dielectrophoresis (cDEP). This study expands the work from our previous report describing for the first time the crossover frequency and cell specific membrane capacitance of different stages of cancer cells that are derived from the same cell line. The specific membrane capacitance increased as the stage of malignancy advanced from 15.39 ± 1.54 mF m^{-2} for a non-malignant benign stage to 26.42 ± 1.22 mF m^{-2} for the most aggressive stage. These differences could be the result of morphological variations due to changes in the cytoskeleton structure, specifically the decrease of the level of actin filaments in the cytoskeleton structure of the transformed MOSE cells. Studying the electrical properties of MOSE cells provides important information as a first step to develop cancer-treatment techniques which could partially reverse the cytoskeleton disorganization of malignant cells to a morphology more similar to that of benign cells. © *2013 American Institute of Physics*. [http://dx.doi.org/10.1063/1.4788921]

I. INTRODUCTION

Ovarian cancer is the most common cause of death arising from gynecological malignancies and is one of the top causes of cancer-related deaths of women in United States and Europe.[1,2] This high rate of mortality is largely a result of the lack of sufficient early cancer detection and efficient treatment techniques. The relative 5-year survival rate for invasive epithelial ovarian cancer patients diagnosed at early stages is more than 90%, while for the late stages it is less than 30%.[3]

Diagnosis and treatment of ovarian cancer in early stages has been hindered by the lack of syngeneic cell models to study this form of cancer at different stages and the inability to isolate early cancer cells from peritoneal fluid. Addressing the lack of adequate cell models, Roberts *et al*. established a progressive mouse ovarian surface epithelial (MOSE) cell model by isolating and culturing ovarian surface epithelial cells; the cells spontaneously transform and progress from a premalignant nontumorigenic to a highly aggressive malignant phenotype.[4,5] This MOSE model enables the study of cellular and molecular changes in different stages of syngeneic ovarian cancer to determine regulatory mechanisms that may drive cancer progression and as such potential targets for cancer diagnosis and treatment.[4] Four stages of the disease were established based on their geno- and phenotype: early (MOSE-E), early intermediate (MOSE-E/I), intermediate (MOSE-I), and late (MOSE-L) cells.[4,5]

[a)]Authors to whom correspondence should be addressed. Electronic addresses: eschmelz@vt.edu and davalos@vt.edu.

It has been shown that benign and cancerous cells are different in many aspects including proliferation, metabolism, cytoskeleton, and other functional categories.[5,6] Some of these differences can lead to distinctions in these cells' electrical properties. It has been reported previously that oral squamous cell carcinomas have distinctly different electrical properties than more normal keratinocyte populations,[7] primary normal keratinocytes, pre-cancerous, dysplastic cells,[8] and non-cancer-derived oral epithelial cells.[9] Additionally, transformed and non-transformed rat kidney cells,[10] malignant human breast cancer epithelial cells and benign breast epithelial cells,[11,12] and healthy and infected erythrocytes have all been shown to have different electrical properties.[13]

Dielectrophoresis (DEP), the motion of a particle due to its polarization in the presence of a non-uniform electric field,[14] has been used to manipulate particles, including mixing,[15] separation,[16–18] enrichment,[19,20] detection,[21] and to investigate their specific electrical properties.[7–13] The dielectrophoretic force can either be positive or negative depending on the applied frequency. Positive dielectrophoresis acts towards regions of high electric field gradient, while negative dielectrophoresis repels particles from the regions of high electric field gradient. There is a frequency, known as crossover frequency, at which the dielectrophoretic force changes sign and the dielectrophoretic force is zero. Electrical properties of cells, such as specific membrane capacitance, can be calculated from their crossover frequency.[22]

Traditionally, the non-uniform electric fields necessary to induce dielectrophoresis are generated by patterning metal electrodes onto the bottom of a microfluidic channel.[23] Alternatively, with the relatively new cell manipulation technique contactless dielectrophoresis (cDEP), metal electrodes are exchanged for conductive fluid electrode channels.[24] These fluid electrode channels are isolated from a main sample channel by a thin insulating membrane. This eliminates direct contact between the sample and the electrodes, preventing bubble formation in the sample channel due to electrolysis, enhancing sterility, and diminishing the effects of electrochemical reactions occurring at the fluid-electrode interface. This technique has recently been used to enrich a population of tumor initiating cells (TICs) from non-tumor initiating cells,[25] to isolate live cells from dead cells,[26] segregate cancer cells from erythrocytes,[27] and separate breast cancer cells from different cell lines based on their metastatic potential.[12]

Typically, ovarian cancers originate from surface epithelial cells of the ovary or fallopian tubes.[28,29] Exfoliated cancer cells can disseminate throughout the peritoneal cavity where they will either form ascites or adhere to the organs or peritoneal lining and begin forming secondary tumors.[4] Addressing the challenge of isolating ovarian cancer cells from peritoneal fluid, we previously demonstrated that a microfluidic approach based on exploitation of cell electrical properties could be useful.[30] We reported that MOSE cell stages ranging from benign to malignant undergo complete trapping at different voltages in the frequency range of 200–600 kHz.[30] The current paper expands the work from our previous study by further investigating the differences in the electrical properties of each cell stage of the MOSE model.

In this study, the crossover frequency of different stages of cancer cells which are derived from the same cell line are reported for the first time. Typically, the rotational (ROT) spectra using quadrapole interdigitated electrodes are used for finding the crossover frequency of cells.[31] Here, we used a recently developed cDEP-based method by Sano *et al.*[32] to find crossover frequency of cells. In this method, a population of cells deflects towards the top (positive DEP) or bottom (negative DEP) half of a microfluidic channel by altering the applied frequency. The crossover frequency is found by observing the frequency at which no deflection occurs. We also investigated the specific membrane capacitance of MOSE cells as they progressed from benign to highly malignant stage. We showed that the electrical properties of a cell are also affected by changes in morphology. This suggests that the cytoskeleton structure could be correlated with bioelectrical characteristics of ovarian cancer cells to provide a transformative approach for characterizing cell progression and phenotypic responses to treatment. Since the changes in electrical properties during progression are associated with the disease phenotype, by studying these changes the outcome of a treatment regimen that affects the cytoskeleton and membrane topography can be predicted. Studying the electrical properties of MOSE cells provides important information as a first step to developing cancer-treatment

techniques that could partially reverse the cytoskeleton disorganization of malignant cells to a morphology more similar to that of benign cells.

II. THEORY

The average DEP force acting on a spherical particle in a non-uniform electric field is given by[33]

$$\vec{F}_{DEP} = p/2.\nabla(\vec{E}_{RMS}.\vec{E}_{RMS}), \tag{1}$$

where p is the effective dipole moment,

$$p = 4\pi\varepsilon_m r^3 Re\{f_{CM}(\omega)\}, \tag{2}$$

ε_m is the media permittivity, r is the radius of the particle, ω is the radial frequency of the electric field, and $\vec{E}_{RMS}$ is the root mean square of the electric field. The Clausius-Mossotti (CM) factor, $f_{CM}(\omega)$, is defined as[33]

$$f_{CM}(\omega) = \frac{\varepsilon_p^* - \varepsilon_m^*}{\varepsilon_p^* + 2\varepsilon_m^*}, \tag{3}$$

where ε^* is the complex permittivity of the particle, subindex p, or suspending medium, subindex m. The complex permittivity is defined as $\varepsilon^* = \varepsilon - j\sigma/\omega$, where ε and σ are the real permittivity and conductivity, respectively, and $j^2 = -1$.

There are numerous methods presented in the literature to model the CM factor of cells.[34–37] Here, we use a single shell model in which a cell is considered as a sphere with interior cytoplasm and a surrounding membrane. The complex permittivity of the cell is defined as a function of the complex permittivity of the membrane, *mem*, and cytoplasm, *cyt*:

$$\varepsilon_p^* = \varepsilon_{mem}^* \frac{\left(\frac{r+d}{r}\right)^3 + 2\left(\frac{\varepsilon_{cyt}^* - \varepsilon_{mem}^*}{\varepsilon_{cyt}^* + 2\varepsilon_{mem}^*}\right)}{\left(\frac{r+d}{r}\right)^3 - \left(\frac{\varepsilon_{cyt}^* - \varepsilon_{mem}^*}{\varepsilon_{cyt}^* + 2\varepsilon_{mem}^*}\right)}, \tag{4}$$

where d is the membrane thickness. The CM factor acts as a scaling function on the magnitude of the DEP force and is theoretically constrained between -0.5 and 1.

For each cell type, within a specific media, there exists a unique frequency at which the cells and media have equivalent complex permittivity, known as the crossover frequency, f_{xo}. At this frequency, the $Re[f_{CM}]$ equals zero, thus there is no net DEP force acting on the cells. When suspended in a low conductivity media (0.01 S m^{-1}), the first crossover frequency of mammalian cells typically occurs between 10 and 100 kHz.[38] Cell size, shape, cytoskeleton, and membrane morphology primarily affect the first crossover frequency of cells.[38,39]

The crossover frequency, f_{xo}, can be found from Eq. (3) by setting $Re\{f_{CM}(\omega)\}$ equal to zero and solving for frequency (ω). f_{xo} can then be found as

$$f_{xo} = \frac{1}{2\pi}\sqrt{\frac{(\sigma_p - \sigma_m)(\sigma_p + 2\sigma_m)}{(\varepsilon_p - \varepsilon_m)(\varepsilon_p + 2\varepsilon_m)}}. \tag{5}$$

The specific capacitance of the cell membrane, C_{mem}, is

$$C_{mem} = \frac{\varepsilon_0 \varepsilon_{mem}}{d}, \tag{6}$$

and the total effective conductance per unit area of the cell membrane, G_{mem}^*, is

$$G^*_{mem} = \frac{2K_{ms}}{r^2} + G_{mem}. \tag{7}$$

ε_0 is the permittivity of the free space, K_{ms} is the surface conductance of the membrane related to the electrical double layer around the cell, and G_{mem} is the conductance associated with the transport of ions across the membrane.[40] Then, Eq. (5) can be simplified to the form of[40]

$$f_{xo} = \frac{\sqrt{2}\sigma_m}{2\pi r C_{mem}} - \frac{\sqrt{2}G^*_{mem}}{8\pi C_{mem}}. \tag{8}$$

It has been shown that for mammalian cells, the second term is negligible considering the conductivity of the media (0.01 S m^{-1} in this study) and the size of the cells.[40] Thus, the crossover frequency can be estimated from

$$f_{xo} = \frac{\sqrt{2}\sigma_m}{2\pi r C_{mem}}. \tag{9}$$

III. MATERIALS AND METHODS

A. Device layout

A top view schematic of the device is shown in Fig. 1. This device includes one sample channel (blue) and three fluid electrode channels (gray) which are separated from the sample channel by 20-μm barriers. Two symmetric electrode channels work as a source and the other electrode channel as a sink. These source and sink electrode channels are 1-cm apart and are filled with phosphate buffered saline (PBS, $\sigma = 1.4$ S m^{-1}). For consistent reference, we will refer to the geometric features of the device as viewed in the top-down schematic shown in Fig. 1. The "top side of the channel" refers to the geometric top half of the channel. The wall in the top half of the sample channel contains the six rounded saw-tooth features which create the non-uniform electric field necessary to induce a DEP force. The "bottom side of the sample channel" refers to the geometric bottom half of the sample channel which is a straight edge. Positive DEP will force cells to the top half of the channel, while negative DEP will push the cells to the bottom half of the sample channel. At the end of the sample channel, there is a T-junction which allows for the collection of cells from one of two outlets. All channels are 50-μm deep.

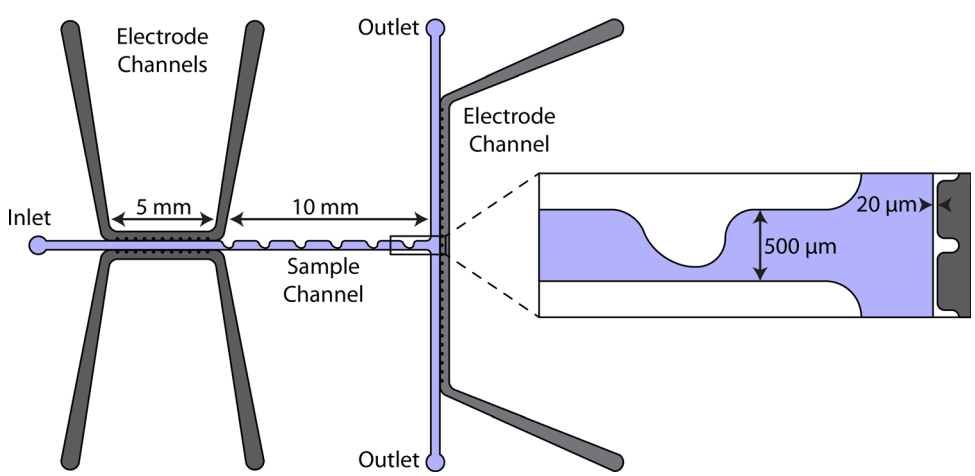

FIG. 1. Top view schematic of the device. Flow is from left to right in the fluidic channel. Inset is a detailed view of a saw-tooth feature and the T-junction.

B. Device fabrication

Microfluidic channels were fabricated in polydimethylsiloxane (PDMS) using soft lithography procedures.[41] For the fabrication of the master stamp, designs were patterned on a silicon wafer by exposing a previously spun photoresist, AZ 9260 (AZ Electronic Materials, Somerville, NJ, USA), to UV light for 60 s through a mask containing the designs. The exposed photoresist was removed by using a developer, AZ 400 K (AZ Electronic Materials, Somerville, NJ, USA), and the silicon master was etched to a depth of 50 μm with deep reactive ion etching (DRIE). The surface roughness due to the DRIE process was removed by wet etching the stamp with tetramethylammonium hydroxide (TMAH) 25% at 70 °C for 5 min. To facilitate the stamping process, a thin layer of Teflon was deposited onto the silicon master using typical DRIE protocols.

Liquid PDMS, in a 10:1 ratio of PDMS monomers and a curing agent (Sylgard 184, Dow Corning, Midland, MI, USA), was degassed under vacuum for one hour and then poured onto the silicon master and cured at 100 °C for 45 min. Solid PDMS was peeled from the stamp and the fluid connections were made with a 1.5 mm puncher (Howard Electronic Instruments, USA). Finally, the PDMS was bonded to a clean glass slide after exposure to air plasma (Harrick Plasma, Ithaca, NY, USA) for 2 min.

C. Cell preparation

MOSE cells, classified by their geno- and phenotype as early (passage number 15–17), early intermediate (passage number 33–34), intermediate (passage number 70–71), and late (passage number 188–189) stage of ovarian cancer were cultured in Dulbecco's Modified Eagle's Medium (DMEM)-high glucose medium supplemented with 4% fetal bovine serum (FBS, Atlanta Biological, Atlanta, GA) and 100 μg/ml each of penicillin and streptomycin, at 37 °C in a humidified atmosphere as described previously.[4,5]

A sugar solution with low electrical conductivity, consisting of 8.5% sucrose [wt vol^{-1}], 0.3% glucose [wt vol^{-1}], and 0.725% [vol vol^{-1}] RPMI[42] was used for the experiments. Each MOSE cell line was harvested by trypsination, washed twice in the sugar solution and then individually resuspended to a concentration of 3×10^6 cells per ml. The final electrical conductivity of the samples, measured prior to each experiment using a conductivity meter (Horiba B-173 Twin Conductivity/Salinity Pocket Testers, Cole-Parmer), was between 0.0094 and 0.0107 S m^{-1}.

Calcein AM, enzymatically converted to green fluorescent calcein, was added to the cell sample at 2 μl per ml of cell suspension to increase the contrast between cells and background for improved data analysis. The radius and viability of cells were measured using the Cell Viability Analyzer (Vi-Cell, Beckman Coulter). The average radius of MOSE-E, -E/I, -I, and -L cells were 7.19 ± 1.00, 7.16 ± 1.25, 7.29 ± 1.49, and 7.05 ± 1.20 μm, respectively (n = 250).

D. Immunofluorescence assay imaging

MOSE cells were seeded on sterile coverslips in a 24-well plate and incubated for 48 h. The cells were fixed with 3% paraformaldehyde in 250 mM HEPES for 10 min, permeabilized with 0.25% triton X100 in 6% paraformaldehyde, and quenched with 50 mM glycine for 10 min. After blocking with 2% BSA in PBS for 1 h, the coverslips were kept in sterile PBS at 4 °C until staining.

The cells were then immunostained to visualize actin filaments and tubulin. Cells were incubated with phalloidin conjugated to Alexa Fluor488 (MolecularProbes, Eugene, OR) for 1 h at room temperature, and washed three times with PBS. They were then incubated with anti-tubulin antibody overnight at 4 °C, followed by incubation with Alexa Fluor 594-conjugated secondary antibody (Molecular Probes) for 1 h at room temperature. After washing three times with PBS, the cells were mounted with Prolong Gold containing DAPI (Invitrogen, Carlsbad, CA) to visualize the nuclei. The images were taken using a Nikon 80i epifluorescence microscope, utilizing UV, FITC, and TRITC filters and a DS-U2 monochromatic camera. NIS

Elements BR 3.0 software (Nikon Instruments, Inc., Melville, NY) was used to capture images and Adobe Photoshop® to process images.

E. Experimental setup

A custom electronics system, based around a LM4780 audio power amplifier (National Semiconductor, Santa Clara, CA), was used to conduct experiments. Two high power audio amplifiers were wired in a parallel push-pull configuration with a gain of 15 yielding a −3 dB bandwidth of 120 kHz. Output voltages, up to 200 V_{RMS}, were produced by driving the output of the amplification stage into a custom wound transformer (AL-T75-V25/300-F20K/120 K, Amp-Line Corp., West Nyack, NY) with a linear output response between 10 and 120 kHz. The system was powered by an unregulated DC power supply with positive and negative output voltage rails at 32 V_{DC} and ripple rejection provided by 10 000 μF capacitors on each rail. The amplitude and frequency of the output signal were controlled using a function generator (GFG-3015, GW Instek, Taipei, Taiwan) and output voltages and frequencies were measured using a high voltage probe (Enhancer 3000, Harvard Apparatus, Inc., Holliston, MA) and oscilloscope (TDS-1002B, Tektronics Inc., Beaverton, OR). For the experiments, the applied voltage was held constant at 200 V_{RMS}. Based on preliminary experiments frequencies were selected in the range of 5 to 35 kHz in 2.5 kHz intervals, and in the range of 40 to 70 kHz in 10 kHz intervals. For each experiment, the frequency was selected at random and experiments were repeated three times with each cell sample.

F. Data analysis

200 V_{RMS} was applied at each frequency for 5 min prior to evaluation to ensure that cells being evaluated traveled the full length of the sample channel. Then, a 2 min video was recorded at the T-junction in the sample channel as shown in the inset of Fig. 1. MATLAB (Version R2010b, The MathWorks Inc., Natick, MA, USA) was used to determine the cell distribution across the width of the channel. At each frequency, the average location of the cells was determined by finding a distribution centerline that resulted in half of the cells being located on each side of the line (the red dashed line in Figs. 2(b), 2(d), and 2(f)). The centerline of the cell distribution was compared to the geometrical centerline of the device to determine if the DEP force was positive or negative. Control experiments were also recorded without an applied voltage to verify that the cells were randomly distributed in the absence of an electric field (Figs. 2(a) and 2(b)). Moreover, electrorotation was not observed during the experiments suggesting that the applied electric field was not sufficient to overcome the friction of the medium to rotate.

The CM factor is theoretically bound between −0.5 and 1. This is visible experimentally in the distribution of cells as they experience positive and negative DEP force (Figs. 2(c) and 2(e)). Because the maximum value of negative DEP force is half of the value of the maximum value of positive DEP force, the cells occupy a relatively wide region on the bottom half of the channel (experiencing negative DEP force) compared to the top half of the channel (experiencing positive DEP force). For each cell type, there is a frequency at which the cells are distributed equally in the top and bottom halves of the channel. At this frequency, the geometric center of the channel matches the line that divides the cell distribution into two equal parts, and this was considered as the crossover frequency.

Since the conductivity of the sample was slightly different for each experiment, the crossover frequency was divided by the experimental sample conductivity, f_{xo}/σ_m, to facilitate comparison between different stages and experimental runs. The specific membrane capacitance was then calculated using Eq. (5), as f_{xo}/σ_m and the average cell radii. These values were compared using the Student's t-test.

G. Computational modeling

The fluid flow in the sample channel was modeled to find the maximum shear rate using the laminar flow module of COMSOL MULTIPHYSICS 4.2 (Comsol Inc., Burlington, MA, USA). A

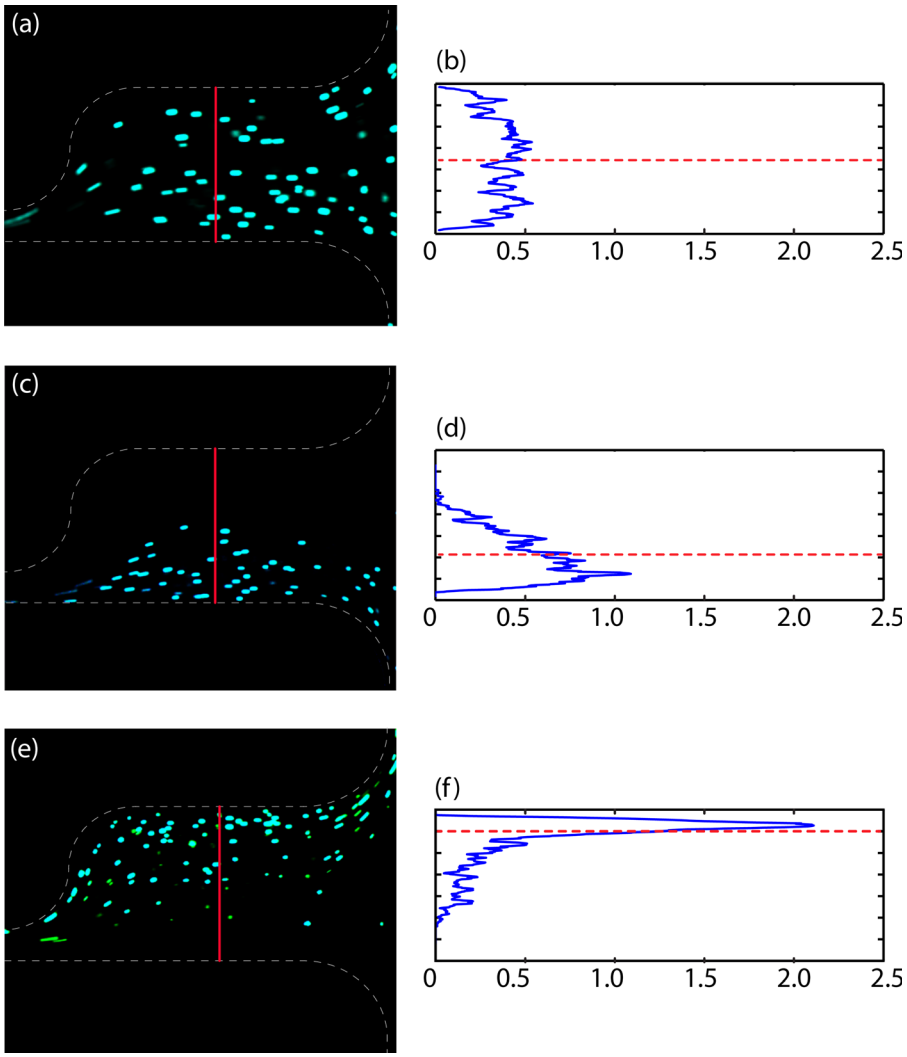

FIG. 2. (a) Control experiments were run without an applied voltage to verify that the cells were randomly distributed in the absence of an electric field; (b) normalized cell distribution from (a). (c) Due to negative DEP force, cells move towards the bottom half of the channel at 10 kHz and 200 V_{RMS}; (d) normalized cell distribution from (c). (e) Due to positive DEP force, cells move towards the top half of the channel at 60 kHz and 200 V_{RMS}; (f) normalized cell distribution from (e). The red solid line in (a), (c), and (e) showed the location that cells distribution was studied. The red dashed line in (b), (d), and (f) shows the center line of the cell distribution.

condition of constant fluid velocity of 56 μm s^{-1} was defined at the inlet boundary to match the experimental volumetric flow rate of 5 μl h^{-1} in the experiments. The sample channel outlets were defined as zero pressure boundaries. The viscosity and density of water, 0.001 Pa.s and 1000 kg m^{-3}, respectively, were used in the main fluidic channel.

Figures 3(a) and 3(b) show the fluid flow and shear rate in the fluidic channel, respectively. The maximum shear rate in the sample channel was found to be approximately 60 s^{-1}. This is two orders of magnitude less than the reported threshold for shear induced cell lysis of approximately 5000 s^{-1}.[43,44]

The electrical potential distribution was modeled using the AC/DC module in COMSOL. Uniform potentials of 200 V were prescribed at the inlet and outlet of the source fluid electrode channels. A ground, or zero potential, boundary condition was applied to the inlet and outlet of the ground fluid electrode channel. The electrical properties of PDMS, defined as $\sigma_{PDMS} = 0.83 \times 10^{-12}$ S m^{-1} and $\varepsilon_{PDMS} = 2.65$, were applied to the domain surrounding the fluid

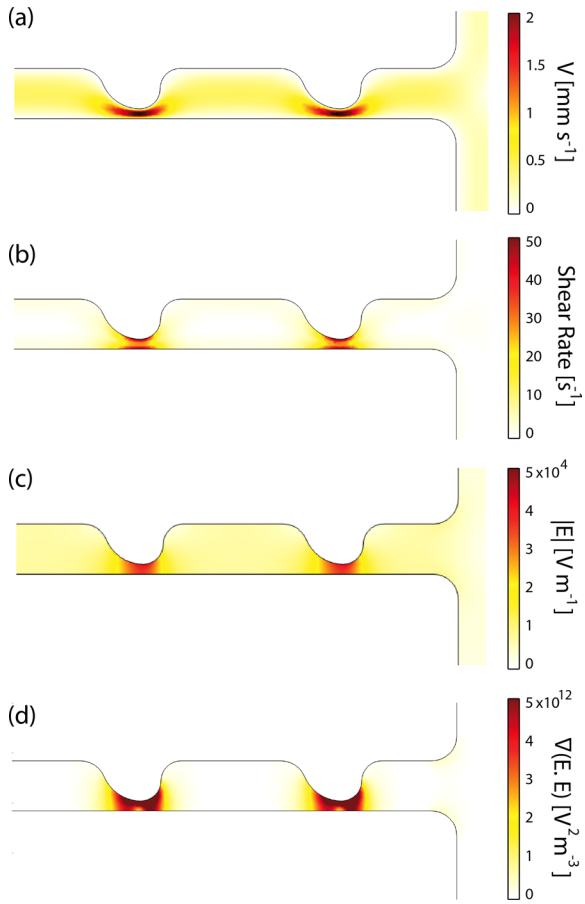

FIG. 3. Computational modeling of the microdevice. Surface plot of (a) the magnitude of the flow velocity (mm s^{-1}), (b) shear rate (s^{-1}), and (c) the magnitude of electric field (V m^{-1}), and (d) gradient of the electric field squared (V^2 m^{-3}) at 200 V_{RMS} and 30 kHz, in the fluidic channel. Flow is from left to right.

channels. The electrical conductivities of PBS and DEP buffer were $\sigma_{PBS} = 1.4\,\mathrm{S\ m^{-1}}$ and $\sigma_{DEP} = 0.01\,\mathrm{S\ m^{-1}}$, respectively, and their relative permittivity was $\varepsilon_{PBS} = \varepsilon_{DEP} = 80$.

Figures 3(c) and 3(d) show the surface plot of the magnitude of electric field and $\nabla(\vec{E}_{RMS} \cdot \vec{E}_{RMS})$, respectively, at 30 kHz. When cells experience a positive DEP force, they will be attracted to higher gradients of electric field squared, $\nabla(\vec{E}_{RMS} \cdot \vec{E}_{RMS})$. When they experience a negative DEP force, they will be repelled from higher $\nabla(\vec{E}_{RMS} \cdot \vec{E}_{RMS})$. As presented by the computational modeling in Fig. 3, $\nabla(\vec{E}_{RMS} \cdot \vec{E}_{RMS})$ is higher at the top side of the sample channel due to the presence of the bumps which generate higher $\nabla(\vec{E}_{RMS} \cdot \vec{E}_{RMS})$. Thus, at lower frequencies (less than the crossover frequency), when cells experience negative DEP, they will be repelled from the top side of the channel and move towards the bottom side (straight edge of the channel), as shown in Fig. 2(c). By increasing the frequency above the crossover frequency, cells experience positive DEP force which causes them to be attracted by higher $\nabla(\vec{E}_{RMS} \cdot \vec{E}_{RMS})$. Due to this, they tend to move towards the top side of the channel (the side of the channel with bumps), as shown in Figure 2(e).

IV. RESULTS AND DISCUSSION

At low frequencies, between 5 and 10 kHz, it was observed that most of the cells were forced into the bottom half of the sample channel, as shown in Fig. 2(c). This indicates that a strong negative DEP force was exerted on the cells. At higher frequencies, above 30 kHz, the cells were forced towards the top half of the device as they experienced a strong positive DEP force (Fig. 2(e)). Figures 2(b), 2(d), and 2(f) present the cells distribution across the red line

shown in Figs. 2(a), 2(c), and 2(e). Since the number of cells crossing the line are not exactly equal in all of the experiments, cell distributions were normalized by the total number of cells crossing the red line in Figs. 2(a), 2(c), and 2(e) to make comparing different experiments cell distributions possible.

The average crossover frequencies, f_{xo}, were 20.14 ± 1.73 kHz, 16.73 ± 0.64 kHz, 16.28 ± 1.07 kHz, 11.90 ± 0.63 kHz for MOSE-E, -E/I, -I, and -L cells, respectively. The crossover frequencies were then divided by the sample conductivity in each experiment, f_{xo}/σ_m, shown in Figure 4(a), to facilitate comparison between different stages and experimental runs. f_{xo}/σ_m for the four stages of MOSE cells are in the same range of values reported previously for different breast cancer cell lines and normal cells.[45,46]

Then, using Eq. (9), area specific membrane capacitances for different stages were calculated as 15.39 ± 1.54, 19.87 ± 0.74, 18.33 ± 2.46, and 26.42 ± 1.22 mF m^{-2} for MOSE-E, E/I, I, and L cells, respectively (Figure 4(b)). C_{mem} increases with progression of the cells from benign early stage to a tumorigenic, malignant state, which is similar to the previously reported behavior of cell lines.[8,10,47–49] The difference in the crossover frequency and cell specific membrane capacitance between MOSE-E and –L ($p < 0.001$), MOSE-E and –E/I ($p < 0.05$ and $p < 0.01$, respectively) and MOSE-I and –L ($p < 0.01$) were statistically significant as determined using Student t-test of three independent experiments. However, the crossover frequency and specific membrane capacitance for MOSE-E/I and –I were not statistically different ($p = 0.27$ and $p = 0.18$, respectively).

A smooth spherical shape cell has been estimated to have a membrane capacitance, C_{mem}, of approximately 9 mF m^{-2}.[31] It has been demonstrated previously that the membrane ruffling of cancer cells is related to increased invasiveness and metastatic potential.[50] This increase in C_{mem} with increased aggressiveness suggests that C_{mem} may be related to the increase in surface protrusions, folds, and ruffling. Moreover, we postulate that the DEP properties of cells can be correlated to the morphological properties of cells in suspension prior to detachment. The literature suggests that the cells maintain their membrane integrity and topography without cytoplasmic leakage during release and detachment.[22] This also connects DEP properties of cells to their cytoskeleton structure of cells before detachment. This is compatible with the observation that MOSE-L cells have more surface protrusions compared to MOSE-E cells in monolayers. MOSE cells progress from the cobblestone-like phenotype seen in MOSE-E cells to the more heterogeneous appearance of MOSE-E/I cells, and finally develop a more spindle-shaped phenotype in the more aggressive stages (MOSE-I, MOSE-L).[4,5] Additionally, membrane protrusions increase as MOSE cells progress to a more aggressive phenotype, which could account for the increase in C_{mem} and consequent decrease in crossover frequency. The gene products that are determinants for the observed bioelectrical properties are subject of further investigation in our laboratories. Future work must be done to validate this.

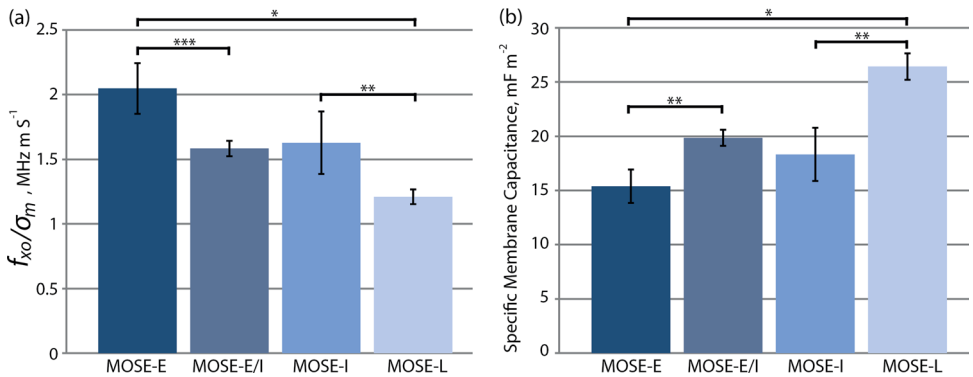

FIG. 4. (a) Crossover frequency and (b) area capacitance of the cell membrane for MOSE-E, -E/I, -I, and -L cells. *, **, and *** represent $p < 0.001$, 0.01, and 0.05, respectively ($n = 3$).

The crossover frequency is affected by cell size and shape, membrane integrity and morphology, and cytoskeleton architecture.[38,39] Since there is no statistical difference in cell size, the changes in crossover frequency at different stages of MOSE cells should be due to other factors, specifically membrane morphology and cytoskeleton. This is supported by previous studies on MOSE cell pheno-and genotypical changes during progression.[4,5] It has been shown that the gene expression in MOSE cells changes in a stepwise manner from MOSE-E to MOSE-I to MOSE-L.[5] The gene expression profiles from transformed stages of MOSE cells have shown significant changes in cell cycle, proliferation, metabolism, and other functional categories which are related to morphological changes and biological behavior of the progressive MOSE cell model.[5] These changes in gene expression levels can directly affect cells' electrical properties by changing membrane morphology and properties of the cytoskeleton and cytoplasm, which can lead to differences in the crossover frequency and specific area capacitance for these cells.

The cytoskeleton organization changes drastically during MOSE progression (Ref. 7 and Figure 5). Variation in cytoskeleton organization can be correlated to alterations in the exterior morphology of cells and consequently with differences in the dielectrophoretic properties of cells.[22] While MOSE-E cells exhibit well-organized actin and tubulin networks, MOSE-L cells have lost the long actin cables and the tubulin organization. This loss of actin stress fibers and tubulin organization may affect the cellular architecture of cancer cells, cellular properties, functions, growth, and signaling events.[5]

Immunofluorescence microscopy was used to determine differences in cells subcellular organization. Figure 5 shows changes in the actin (green) and tubulin (red) organization during MOSE progression and confirms the loss of actin stress fibers and tubulin organization that affect the cellular architecture of cancer cells, cellular properties, functions, growth, and signaling events.[5] We have shown previously that the concentration of f-actin is also higher in MOSE-E cells. Moreover, a significant decrease in tubulin organization was observed. In MOSE-E cells the α- and β-tubulin are long filaments which are a normal structure in epithelial cells. However, MOSE-L cells have a random disorganized filaments structure.[5] These results are in agreement with the changes in morphology and surface protrusion of the cells which will consequently change the cells membrane capacitance. In addition, membrane blebbing has been linked to cortical actin, which lies beneath the plasma membrane.[51] Thus, changes in the cells cortical cytoskeleton during MOSE cell progression may directly impact the dielectrophoretic properties of cells. This will be further investigated in our future studies.

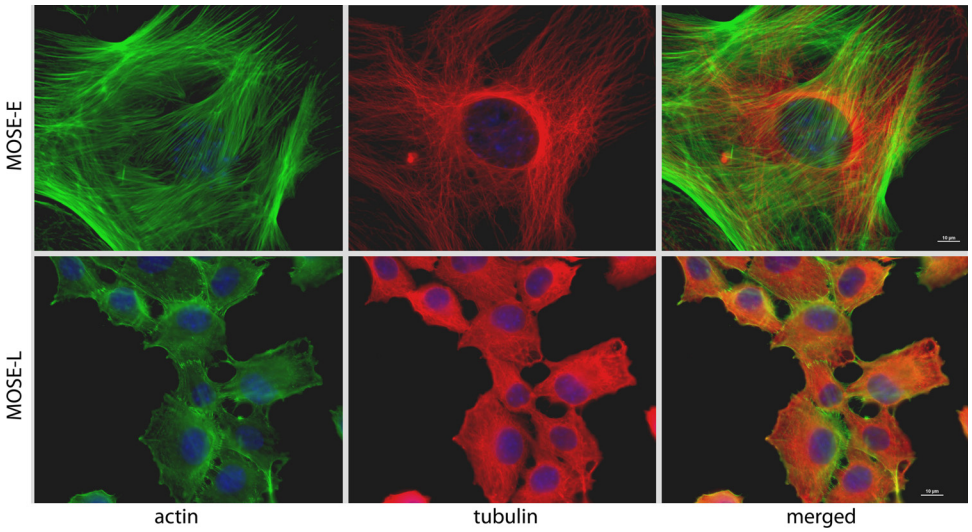

FIG. 5. Organization of the cytoskeleton during MOSE neoplastic progression. Triple immunofluorescent staining of MOSE-E and MOSE-L cells to visualize actin filaments (phalloidin, green), tubulin filaments (red), and nucleus (DAPI, blue).

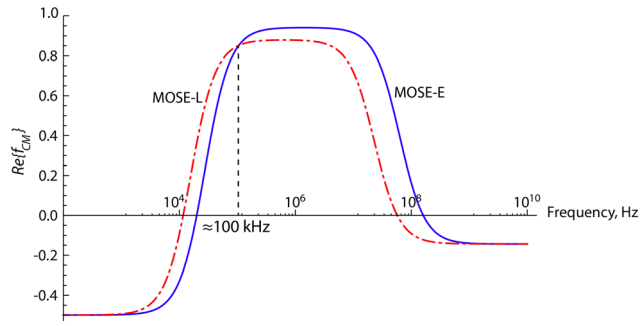

FIG. 6. Clausius-Mossotti factor of MOSE-E and MOSE-L cells as a function of frequency using Equation (3). The previously reported values for cancer cells were used for both early and late stages: cell membrane relative permittivity, 10^{-8},[37] membrane thickness, 5 nm,[52] cytoplasm relative permittivity, 60.[53] The cytoplasm conductivity of MOSE-E and MOSE-L cells were approximated as 0.71 and 0.25 S m^{-1}, respectively.[8] Media permittivity and conductivity are $\varepsilon_m = \varepsilon_{DEP} = 80$ and $\sigma_m = \sigma_{DEP} = 0.01$, respectively.

By substituting measured cell radius and crossover frequency, using the calculated values for specific membrane capacitance and previously reported values for cancer cell membrane relative permittivity (10^{-8}),[37] membrane thickness (5 nm),[52] cytoplasm relative permittivity (60),[53] and knowing the media permittivity and conductivity, $\varepsilon_m = \varepsilon_{DEP} = 80$ and $\sigma_m = \sigma_{DEP} = 0.01$ S m^{-1}, respectively, the real part of Clausius-Mossotti factor for different stages of MOSE cells can be predicted as a function of frequency using Eqs. (3) and (4). The cytoplasm conductivity of MOSE-E and MOSE-L cells were approximated 0.71 and 0.25 S m^{-1}, respectively.[8] The real part of Clausius-Mossotti factors, $Re\{f_{CM}(\omega)\}$, for early and late stages of MOSE cells are shown in Fig. 6.

As shown in Fig. 6, $Re\{f_{CM}\}$ of MOSE-E is larger than $Re\{f_{CM}\}$ of MOSE -L at frequencies higher than approximately 100 kHz. This predicts that a higher voltage is required to trap MOSE-L cells compared to MOSE-E cells at a constant frequency which is in agreement with our previous studies at the frequency range of 200-500 kHz.[30] This result support our previous study's prediction that it can be possible to separate MOSE-L cells from MOSE-E cells, as well as peritoneal cells, macrophages and fibroblasts, which have DEP properties more similar to MOSE-E cells,[30] for selectively screening of ovarian cancer cells.

V. CONCLUSIONS

In this study, the crossover frequency and specific membrane capacitance of different stages of MOSE cells were calculated using a relatively new cell sorting technique known as contactless dielectrophoresis (cDEP). We found that the specific membrane capacitance of MOSE cells increases as the cells progress from a benign stage to more malignant stages. These differences may be due to the morphological differences and changes in the cytoskeleton of these cells as they transition to a more aggressive phenotype. These results indicate that cDEP can be used to study cell membrane properties and the differences between membranes of different cell lines, specifically between individual stages of cancer cells or differentiated cells. This study also advanced our knowledge of ovarian cancer progression by characterizing the electrical properties of MOSE cells. This transformative research provided previously unknown information as to the electrical properties of a syngeneic ovarian cancer cell model, which may lead to more effective early detection and cancer-treatment techniques.

ACKNOWLEDGMENTS

This material is based upon work supported in part by the National Science Foundation under Grant No. EFRI 0938047, by the Virginia Tech Institute for Critical Technology and Applied Science (ICTAS), and by NIH RO1 CA118846 (to EMS and PCR). The authors would like to thank Dr. Mark A. Stremler, Bioelectromechanical Systems (BEMS) laboratory member, Elizabeth Savage, and Dr. Schmelz laboratory member, Amanda Shea, for their contributions.

[1]I. Visintin, Z. Feng, G. Longton, D. C. Ward, A. B. Alvero, Y. Lai, J. Tenthorey, A. Leiser, R. Flores-Saaib, H. Yu, M. Azori, T. Rutherford, P. E. Schwartz, and G. Mor, Clin. Cancer Res. **14**, 1065–1072 (2008).
[2]I. J. Jacobs and U. Menon, Mol. Cell Proteomics **3**, 355–366 (2004).
[3]A. Jemal, R. Siegel, J. Xu, and E. Ward, CA Cancer J. Clin **60**, 277–300 (2010).
[4]P. C. Roberts, E. P. Mottillo, A. C. Baxa, H. H. Heng, N. Doyon-Reale, L. Gregoire, W. D. Lancaster, R. Rabah, and E. M. Schmelz, Neoplasia **7**, 944–956 (2005); available at http://www.ncbi.nlm.nih.gov/pmc/articles/PMC1502030/.
[5]A. L. Creekmore, W. T. Silkworth, D. Cimini, R. V. Jensen, P. C. Roberts, and E. M. Schmelz, PLoS ONE **6**, e17676 (2011).
[6]D. Hanahan and R. A. Weinberg, Cell **144**, 646–674 (2011).
[7]L. M. Broche, N. Bhadal, M. P. Lewis, S. Porter, M. P. Hughes, and F. H. Labeed, Oral Oncol. **43**, 199–203 (2007).
[8]H. J. Mulhall, F. H. Labeed, B. Kazmi, D. E. Costea, M. P. Hughes, and M. P. Lewis, Anal. Bioanal. Chem. **401**, 2455–2463 (2011).
[9]L. Yang, L. R. Arias, T. S. Lane, M. D. Yancey, and J. Mamouni, Anal. Bioanal. Chem. **399**, 1823–1833 (2011).
[10]Y. Huang, X. B. Wang, F. F. Becker and P. R. Gascoyne, Biochim. Biophys. Acta **1282**, 76–84 (1996).
[11]J. An, J. Lee, S. H. Lee, J. Park, and B. Kim, Anal. Bioanal. Chem. **394**, 801–809 (2009).
[12]E. A. Henslee, M. B. Sano, A. D. Rojas, E. M. Schmelz, and R. V. Davalos, Electrophoresis **32**, 2523–2529 (2011).
[13]T. Braschler, N. Demierre, E. Nascimento, T. Silva, A. G. Oliva, and P. Renaud, Lab Chip **8**, 280–286 (2008).
[14]H. A. Pohl, *Dielectrophoresis: The Behavior of Neutral Matter in Nonuniform Electric Fields* (Cambridge University Press, Cambridge, 1978).
[15]A. Salmanzadeh, H. Shafiee, R. V. Davalos, and M. A. Stremler, Electrophoresis **32**, 2569–2578 (2011).
[16]B. H. Lapizco-Encinas, B. A. Simmons, E. B. Cummings, and Y. Fintschenko, Anal. Chem. **76**, 1571–1579 (2004).
[17]G. H. Markx, M. S. Talary, and R. Pethig, J. Biotechnol. **32**, 29–37 (1994).
[18]K. H. Kang, Y. Kang, X. Xuan, and D. Li, Electrophoresis **27**, 694–702 (2006).
[19]H. Shafiee, J. L. Caldwell, and R. V. Davalos, J. Assoc. Lab. Autom. **5**, 224–232 (2010).
[20]M. Stephens, M. S. Talary, R. Pethig, A. K. Burnett, and K. I. Mills, Bone Marrow Transpl. **18**, 777–782 (1996).
[21]Z. Gagnon and H. C. Chang, Electrophoresis **26**, 3725–3737 (2005).
[22]P. R. C. Gascoyne, S. Shim, J. Noshari, F. F. Becker, and K. Stemke-Hale, "Correlations between the dielectric properties and exterior morphology of cells revealed by dielectrophoretic field-flow fractionation," Electrophoresis (to be published).
[23]C. F. Gonzalez and V. T. Remcho, J. Chromatogr. A **1079**, 59–68 (2005).
[24]H. Shafiee, J. L. Caldwell, M. B. Sano, and R. V. Davalos, Biomed. Microdevices **11**, 997–1006 (2009).
[25]A. Salmanzadeh, L. Romero, H. Shafiee, R. C. Gallo-Villanueva, M. A. Stremler, S. D. Cramer, and R. V. Davalos, Lab Chip **12**, 182–189 (2012).
[26]H. Shafiee, M. B. Sano, E. A. Henslee, J. L. Caldwell, and R. V. Davalos, Lab Chip **10**, 438–445 (2010).
[27]M. B. Sano, J. L. Caldwell, and R. V. Davalos, Biosens Bioelectron. **30**, 13–20 (2011).
[28]N. Auersperg, T. Ota, and G. W. Mitchell, Int. J. Gynecol. Cancer **12**, 691–703 (2002).
[29]K. Sundfeldt, Mol. Cell Endocrinol. **202**, 89–96 (2003).
[30]A. Salmanzadeh, H. Kittur, M. B. Sano, C. R. P. E. M. Schmelz, and R. V. Davalos, Biomicrofluidics **6**, 024104 (2012).
[31]W. M. Arnold and U. Zimmermann, Naturwiss. **69**, 297–298 (1982).
[32]M. B. Sano, E. A. Henslee, E. Schmelz, and R. V. Davalos, Electrophoresis **32**, 3164–3171 (2011).
[33]H. A. Pohl, *Dielectrophoresis* (Cambridge University Press, 1978).
[34]X. B. Wang, Y. Huang, P. R. Gascoyne, F. F. Becker, R. Holzel, and R. Pethig, Biochim. Biophys. Acta **1193**, 330–344 (1994).
[35]K. V. Kaler and T. B. Jones, Biophys. J. **57**, 173–182 (1990).
[36]Y. Huang, R. Holzel, R. Pethig, and X. B. Wang, Phys. Med. Biol. **37**, 1499–1517 (1992).
[37]P. Marszalek, J. J. Zielinsky, M. Fikus, and T. Y. Tsong, Biophys. J. **59**, 982–987 (1991).
[38]R. Pethig, in *BioMEMS and Biomedical Nanotechnology* (SpringerLink, 2007), pp. 103–126.
[39]R. Pethig, A. Menachery, S. Pells, and P. De Sousa, J. Biomed. Biotechnol. **2010**, 182581 (2010).
[40]R. Pethig and M. S. Talary, IET Nanobiotechnol. **1**, 2–9 (2007).
[41]D. J. Beebe, G. A. Mensing, and G. M. Walker, Annu. Rev. Biomed. Eng. **4**, 261–286 (2002).
[42]L. A. Flanagan, J. Lu, L. Wang, S. A. Marchenko, N. L. Jeon, A. P. Lee, and E. S. Monuki, Stem Cells **26**, 656–665 (2008).
[43]R. C. Skalak and S. Chien, *Handbook of Bioengineering* (McGraw-Hill, New York, 1987).
[44]Y. C. P. Fung, N. Perrone, and M. Anliker, *Biomechanics, Its Foundations and Objectives* (Prentice-Hall, Englewood Cliffs, NJ, 1972).
[45]P. R. Gascoyne, X. B. Wang, Y. Huang, and F. F. Becker, IEEE Trans. Appl. Ind. **33**, 670–678 (1997).
[46]A. Han, L. Yang, and A. B. Frazier, Clin. Cancer Res. **13**, 139–143 (2007).
[47]P. R. C. Gascoyne, J. Noshari, F. F. Becker, and R. Pethig, IEEE Trans. Appl. Ind. **30**, 829–834 (1994).
[48]F. F. Becker, X. B. Wang, Y. Huang, R. Pethig, J. Vykoukal, and P. R. C. Gascoyne, J. Phys. D: Appl. Phys. **27**, 2659–2662 (1994).
[49]F. F. Becker, X. B. Wang, Y. Huang, R. Pethig, J. Vykoukal, and P. R. Gascoyne, Proc. Natl. Acad. Sci. USA **92**, 860–864 (1995).
[50]W. G. Jiang, Eur. J. Surg. Oncol. **21**, 307–309 (1995).
[51]J. Y. Tinevez, U. Schulze, G. Salbreux, J. Roensch, J. F. Joanny, and E. Paluch, Proc. Natl. Acad. Sci. USA **106**, 18581–18586 (2009).
[52]R. Pethig and D. B. Kell, Phys. Med. Biol. **32**, 933–970 (1987).
[53]R. Pethig, Biomicrofluidics **4**(2), 022811 (2010).